AIP | Review of Scientific Instruments

Fast temperature spectrometer for samples under extreme conditions

Dongzhou Zhang, Jennifer M. Jackson, Jiyong Zhao, Wolfgang Sturhahn, E. Ercan Alp, Thomas S. Toellner, and Michael Y. Hu

Citation: Review of Scientific Instruments **86**, 013105 (2015); doi: 10.1063/1.4905431
View online: http://dx.doi.org/10.1063/1.4905431
View Table of Contents: http://scitation.aip.org/content/aip/journal/rsi/86/1?ver=pdfcov
Published by the AIP Publishing

Fast temperature spectrometer for samples under extreme conditions

Dongzhou Zhang,[1,2,a)] Jennifer M. Jackson,[1] Jiyong Zhao,[2] Wolfgang Sturhahn,[1] E. Ercan Alp,[2] Thomas S. Toellner,[2] and Michael Y. Hu[2]
[1]*Seismological Laboratory, California Institute of Technology, Pasadena, California 91125, USA*
[2]*Advanced Photon Source, Argonne National Laboratory, Argonne, Illinois 60439, USA*

(Received 1 July 2014; accepted 20 December 2014; published online 13 January 2015)

We have developed a multi-wavelength Fast Temperature Readout (FasTeR) spectrometer to capture a sample's transient temperature fluctuations, and reduce uncertainties in melting temperature determination. Without sacrificing accuracy, FasTeR features a fast readout rate (about 100 Hz), high sensitivity, large dynamic range, and a well-constrained focus. Complimenting a charge-coupled device spectrometer, FasTeR consists of an array of photomultiplier tubes and optical dichroic filters. The temperatures determined by FasTeR outside of the vicinity of melting are, generally, in good agreement with results from the charge-coupled device spectrometer. Near melting, FasTeR is capable of capturing transient temperature fluctuations, at least on the order of 300 K/s. A software tool, SIMFaster, is described and has been developed to simulate FasTeR and assess design configurations. FasTeR is especially suitable for temperature determinations that utilize ultra-fast techniques under extreme conditions. Working in parallel with the laser-heated diamond-anvil cell, synchrotron Mössbauer spectroscopy, and X-ray diffraction, we have applied the FasTeR spectrometer to measure the melting temperature of $^{57}Fe_{0.9}Ni_{0.1}$ at high pressure. [http://dx.doi.org/10.1063/1.4905431]

I. INTRODUCTION

Accurate and precise temperature determinations are among several important factors in obtaining reliable thermodynamic data for materials from experiments under extreme pressures and temperatures. In high pressure experiments conducted using the diamond-anvil cell (DAC), there are three common ways to reach high temperatures: laser heating,[1–4] resistive heating,[5–7] and shock-wave loading of precompressed samples.[8,9] The latter method permits unique states of matter to be probed at high pressures and temperatures. However, the sample is typically destroyed, thus presenting reproducibility challenges.[9] Heating by infrared (IR) lasers permits temperatures characteristic of Earth's deep interior to be reached (up to and exceeding 6500 K). Although resistive heating alone presents challenges in generating temperatures higher than 2000 K at high pressures,[5–7] thermocouple-based temperature determinations provide fairly accurate and precise sample temperatures. Laser heating can be implemented in most DAC designs, while special gaskets, additional heaters, and associated controllers are required for resistive heating.[5–7] Laser heating is, therefore, often employed in high pressure experiments where temperatures greater than about 1200 K are desired.

Laser heating does present challenges. The temperature distribution in laser heating experiments can be inhomogeneous.[10,11] Some recent progress has been made in increasing the spatial homogeneity, including laser heating from both sides,[1,4] combining different laser modes,[1] and adjustable laser geometry with beam-shaping optics.[4] The second and less discussed challenge is the stability of laser heating over a defined time period. The sample temperature in a laser heating experiment can fluctuate faster than in resistive heating experiments. Previous studies have documented temperature fluctuations of several hundred Kelvins[12–16] at a minimum of tens of Hz[12] during continuous wave laser heating. Experiments have shown that small (~0.2%-3%) temporal fluctuations in laser power are followed by large fluctuations in the temperature of the sample.[12] It is also suggested that melting of the thermal insulation layer,[15] changes in the thermal conductivity in the sample chamber,[17] and changes in the laser coupler's reflectivity[17] may contribute to these large temperature fluctuations. Such fluctuations are not favorable for reliable temperature determinations of a laser-heated sample, and will inevitably increase the uncertainty of the temperature measurement.

There are a few approaches to address unstable temperature readouts in laser-heated DAC experiments. Closed-loop laser power feedback systems have proved to be effective in reducing the temperature fluctuation at a constant laser power.[1,18] However, this method is not suitable for experiments that involve ramping up the laser power every few seconds, such as that done for melting studies. For these types of experiments, it is preferred to determine the temperature of the sample at a frequency higher than the sample's temperature fluctuations and the accumulation time needed to diagnose certain material properties (in this case, melting). Currently, most temperature determination systems in laser-heated DAC experiments use charge-coupled device (CCD) chips as detectors. The CCD chip is either used in a spectrometer to fit the measured intensities to a temperature using Planck's law[1,4,19] or used to monitor the spatial distribution of the hotspot temperature by measuring the intensities of different wavelength bands.[11,20] However, conventional CCD

a)dzzhang@caltech.edu

spectrometers have some limitations, including a low dynamic range. The dynamic range of a modern CCD spectrometer is on the order of 10^3-10^4 for a single acquisition (e.g., Ocean Optics USB-4000), whereas the dynamic range of the photomultiplier tube (PMT) is $\sim 10^6$. The large dynamic range is important for an accurate determination of the temperature. Another limitation of many CCD-based spectrometers is a slow reading rate. The conventional CCD chips for spectrometers usually have 10^3-10^5 pixels. To calculate the temperature using the CCD data, first one needs to read the intensity from the CCD chip, and then transfer the entire CCD image to the controlling computer to compute the temperature. In most CCD-equipped laser-heated DAC experiments at the synchrotron, the temperature readout frequency is at best on the order of 1 Hz (e.g., Dewaele *et al.*[14,15] and Anzellini *et al.*[16]). For laser-heated DAC experiments involving time-resolution and rapid temperature changes, a high-frequency accurate temperature readout system with a large dynamic range is highly desirable.

In this study, we present a new multi-wavelength **Fas**t **Te**mperature **R**eadout (FasTeR) spectrometer operating in-line with nuclear resonant scattering (NRS) and X-ray diffraction (XRD) techniques at the Advanced Photon Source at Argonne National Laboratory. FasTeR is dedicated to experiments involving rapid temperature changes in the sample near its solidus,[21] and is tailored to laser-heated DACs. The FasTeR spectrometer may be combined with other time-resolved measurements, such as time-domain thermoreflectance,[22–24] thermal diffusivity,[25] measurements using the dynamic diamond-anvil cell,[26] pulsed laser-heating,[27,28] high-speed shutter-based techniques,[29] and perhaps even shock/ramp compression experiments.[8,9,30]

II. INSTRUMENTATION

A. Experimental set-up

The fast temperature readout system described in this paper is installed at beamline 3-ID-B at the Advanced Photon Source of Argonne National Laboratory. It operates in parallel with NRS methods, XRD, laser heating, and a conventional CCD-based temperature readout system (Fig. 1). Previous reports have described the experimental set-up for NRS and XRD studies at this beamline,[19,21,31] and the principles of NRS have been described before in detail.[32] In this study, we combine a new multi-wavelength FasTeR spectrometer with synchrotron Mössbauer spectroscopy (SMS), also known as nuclear resonant forward scattering, and X-ray diffraction to determine the melting temperature of $^{57}Fe_{0.9}Ni_{0.1}$ at high pressure. In the following paragraphs, the details of the experimental set-up are described.

The X-rays are first monochromatized by a high heat-load diamond-crystal monochromator to a bandwidth of 1 eV, then filtered to the bandwidth of 1 meV using a silicon multiple-crystal Bragg reflection monochromator.[33] Two Kirkpatrick-Baez mirrors, one horizontal and the other vertical, are used to obtain a measured optimal X-ray focal spot size of $\sim$10(horizontal)×11(vertical) μm^2 at the full width at half maximum. The storage ring is operated in a low-emittance

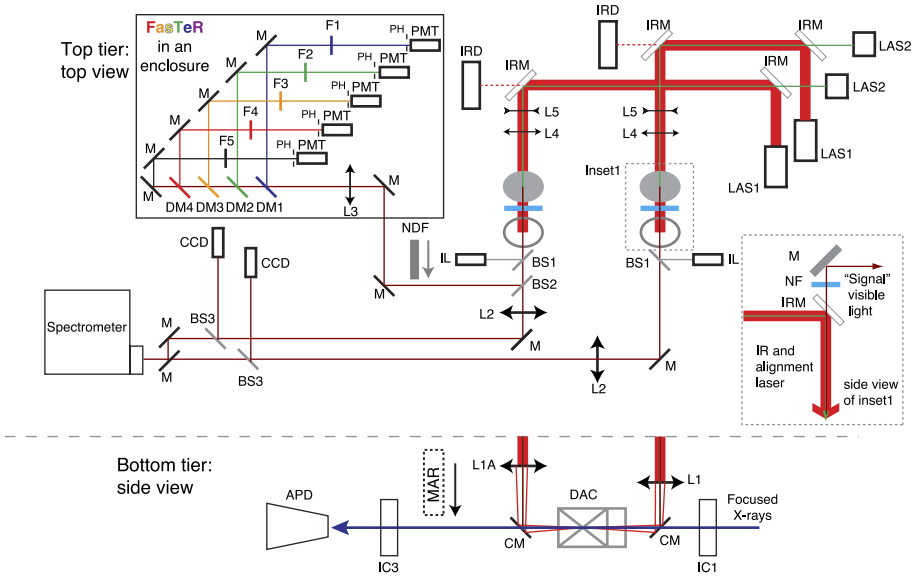

FIG. 1. Design of the experimental set-up for laser-heating, nuclear resonant scattering, X-ray diffraction, and FasTeR at beamline 3-ID-B of the Advanced Photon Source at Argonne National Laboratory. LAS1: 100 W continuous fiber laser, 1064 nm (IPG Photonics). The power supplies are located outside of the experimental station. LAS2: 1 mW 532 nm alignment laser (Lasermate). IRM: 1064 nm coated infrared laser mirror (Newport). M: Al-coated flat mirror (ThorLabs). CM: amorphous carbon mirror with silver coating. IRD: infrared pindiode. NF: 1064 nm notch filter. L1: 100 mm focal-length apochromat lens (Sigma Optics). L1A: 77 mm focal-length apochromat lens (USLaser). L2: 1m focal-length achromat lens (Oriel). L3: 700 mm focal-length achromat lens (CVI Melles-Griot). L4: 100 mm focal-length planoconvex lens (ThorLabs). L5: −25 mm focal-length planoconcave lens (ThorLabs). L4 and L5 together form the beam size controller. IL: 18 W LED illuminator (Schott). BS1: 92-8 pellicle beamsplitter (ThorLabs). BS2: 50-50 metallic beamsplitter (OFR). BS3: 45-55 coated pellicle beam splitter (ThorLabs). DM1-4: dichroic beamsplitters for different wavelength bands (Semrock). F1-5: bandpass filters for different wavelength bands (Semrock). PH: 50 μm pinhole (Edmund optics). PMT: photomultiplier tube (Hamamatsu). NDF: optical density 2.0 neutral density filter (ThorLabs). CCD: charge-coupled device camera (Panasonic). Spectrometer: $f/2.2$ broadband grating spectrometer with a 1024 × 250 pixel front illuminated CCD (Princeton Instrument). IC1: ion chamber with Ne gas. IC3: ion chamber with Ar gas. APD: avalanche photodiode detector. MAR: X-ray image plate on a horizontal moving stage (Marresearch GmbH). DAC: diamond-anvil cell. The perspectives of the top tier and the bottom tier are perpendicular to each other.

top-up mode with 24 bunches that are separated by 153 ns. Two ion chambers are placed in the upstream (IC1) and the downstream (IC3) sides of the sample stage to monitor the X-ray intensity before and after the sample (Fig. 1, bottom tier). XRD measurements are carried out using a moveable mar345 Image Plate Detector System (Marresearch GmbH). The image plate is placed ~300 mm away from the sample in the downstream direction. Ambient CeO_2 is used to calibrate the position and tilt of the image plate. *In-situ* XRD patterns ($E = 14.4125$ keV, $\lambda = 0.86025$ Å) are typically collected at each compression point to obtain the unit-cell volume of the sample, which can then be used with an appropriate equation of state to determine the pressure of the sample.

The double-sided IR laser heating system at beamline 3-ID-B is similar to systems installed at beamlines 16-ID-B (HPCAT)[3] and 13-ID-D (GSE-CARS)[4] of the APS. Upgrades to the double-sided laser-heating system at 3-ID-B[19] are described here, and they include two randomly polarized diode-pumped fiber lasers (IPG Photonics, 100 W each) with remote power control. These two lasers are single-mode continuous wave ytterbium-doped lasers working at a wavelength of 1064 nm. Located on a table above the X-ray beam (Fig. 1, top tier), the IR laser heads with co-axial green alignment lasers (Lasermate, 532 nm, 1 mW) are guided to the sample position with mirrors. A pair of 100 mm focal length convex and −25 mm focal length concave lenses (ThorLabs) is used to regulate the divergence and size of the IR laser beams. The distance between the two lenses is controlled remotely by stepping motors, so that the IR laser hotspot diameter ($Ø_{laser}$) is adjustable between approximately 15 and 50 μm. The IR laser has a Gaussian intensity profile. On the bottom tier, two different apochromats are used to focus the laser beams on the sample. These apochromats are optimized for both IR and visible light to minimize the chromatic aberration. The apochromat in the upstream direction of the sample (OptoSigma) has a focal length of 100 mm. In the downstream direction, an apochromat with a 77 mm focal length (USLaser) is used. A pair of amorphous graphite mirrors coated with silver is used to guide the IR laser beams. The amorphous graphite mirrors minimize the attenuation of the incident X-rays onto the sample. A conventional broadband grating CCD spectrometer (1024×250 pixels, Princeton Instrument) determines the temperature from the upstream and downstream sides of the heated sample,[19] thus monitoring the presence of axial surface temperature gradients.

B. FasTeR

The design of the FasTeR spectrometer described here was originally developed for shock compression experiments.[30] FasTeR utilizes sensitive detectors at select wavelength ranges in the visible regime to sample the thermal radiation of hotspot in a laser-heated diamond anvil cell. The typical sizes of these hotspots are on the order of ~40 μm, significantly smaller than those in the shock wave experiments.[30] For example, the system by Lyzenga and Ahrens[30] is capable of determining shock temperatures as fast as every ~10 ns, with a field of view (Ø) of 1 mm^2. The field of view for FasTeR ($Ø_{FasTeR}$) is determined from the magnification ratio of the two apochromats (700 mm : 77 mm) and the 50 μm pinhole in front of the detectors (Fig. 1, inset 2), resulting in $Ø_{FasTeR} = 6$ μm. The intensity ratio between these different wavelength bands is computed and used with Planck's law to determine the temperature of the sample. The details of FasTeR are laid out in the following paragraphs.

The FasTeR spectrometer consists of an array of PMTs (Hamamatsu) as detectors. PMTs combine high gain, low noise, and high frequency response. They have a working frequency of 20 kHz, a radiant sensitivity of ~200 V/nW, and a large dynamic range (~10^6). A neutral density filter (NDF, ThorLabs, optical density 2.0) can be moved in to the optical path in order to prevent saturation of the PMTs, when the hotspot emission has a high intensity. The NDF gives two additional orders of magnitude to the total dynamic range of FasTeR, and it can be added remotely by computer control during an experiment.

The optical filters are essential in our temperature determination, because they define the transmission bands in the visible spectrum. To obtain five distinct, non-overlapping bands distributed between 350 nm and 850 nm, FasTeR uses four 45° dichroic mirrors (Semrock), one mirror (Newport), and five vertical incident bandpass filters (Semrock) (Fig. 2). Each of these bands is ~40 nm wide, with edges sharper than 5 nm. The transmission of each band is higher than 85%, and the signal of each band is collected by one individual PMT. The photocathodes of PMTs are selected to suit their corresponding optical transmission bands. Though the incident signal is passing through a 45° tilted infrared mirror, which is 5 mm thick (Fig. 1, inset 1), the chromatic aberration is very low for our FasTeR system because each PMT detector is collecting the signal from only one transmission band, and each transmission band is ~40 nm wide. The chromatic aberration in each band is smaller than 4 μm on the detector side, which leads to a

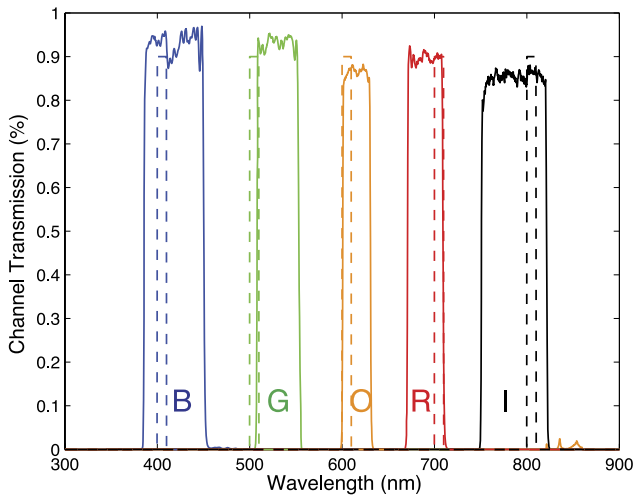

FIG. 2. Wavelength-dependent channel transmission of the optical bandpass filters for FasTeR. B: blue channel (386-450 nm). G: green channel (508-553 nm). O: orange channel (601-631 nm). R: red channel (671-709 nm). I: infrared channel (751-821 nm). Solid curves: channel transmission used in experiments. These curves are based on the data provided by the manufacturer of the mirrors and filters. Dashed curves: For example, 10 nm bandwidth channel transmission used in simulation (please refer to Figs. 7(e) and 7(f) for more details).

temperature error of less than 10 K. The optical signal received by each PMT is referred to as a "channel." Currently, there are five channels in the FasTeR system: the blue channel (B: 386-450 nm), green channel (G: 508-553 nm), orange channel (O: 601-631 nm), red channel (R: 671-709 nm), and infrared channel (I: 751-821 nm). From the convolution of Planck's law and the channel transmission, the theoretical intensity ratios between different channels can be calculated. See Sec. II C for details on temperature calibration.

Stepping motors are used to align and focus the five PMTs to the same position. The resolution of the stepping motor is 1 μm in three translational dimensions. During the aligning and focusing procedure, we place a 25 μm pinhole at the measured X-ray focus position, and illuminate the pinhole uniformly from the back. We then scan the pinhole in three orthogonal directions (x,y,z), and fine-tune the position of the pinhole's image on the PMTs by adjusting the angles of the reflection mirrors and the positions of the PMTs, such that the signals are maximized when the pinhole is at the X-ray focus position. This procedure guarantees the alignment and focus of the FasTeR system with respect to the X-ray focus.

C. Calibration

Accurate determinations of temperature using FasTeR require that the responses of each channel at different temperatures are known. To calibrate these responses, we use a frosted-glass tungsten ribbon standard lamp with known radiance (Gigahertz-Optik). The working temperature range of this lamp is between 2000 K and 3200 K, and its temperature has been calibrated against the input current at the National Institute for Standards and Technology. During the calibration, we place a 25 μm pinhole at the X-ray focus position. The standard lamp is fixed 10 cm away from the pinhole, illuminating the pinhole uniformly from the back. At a certain temperature of the standard lamp, an average intensity over 30 s is recorded as a particular channel's response. Calibrations with NDF in and out of the optical path are carried out independently. We measure the five channels' responses throughout the lamp's working temperature range (Fig. 3).

To compute the hotspot temperature, we use the relative ratio between channels instead of the absolute intensity from each channel. The theoretical relative ratio curves between

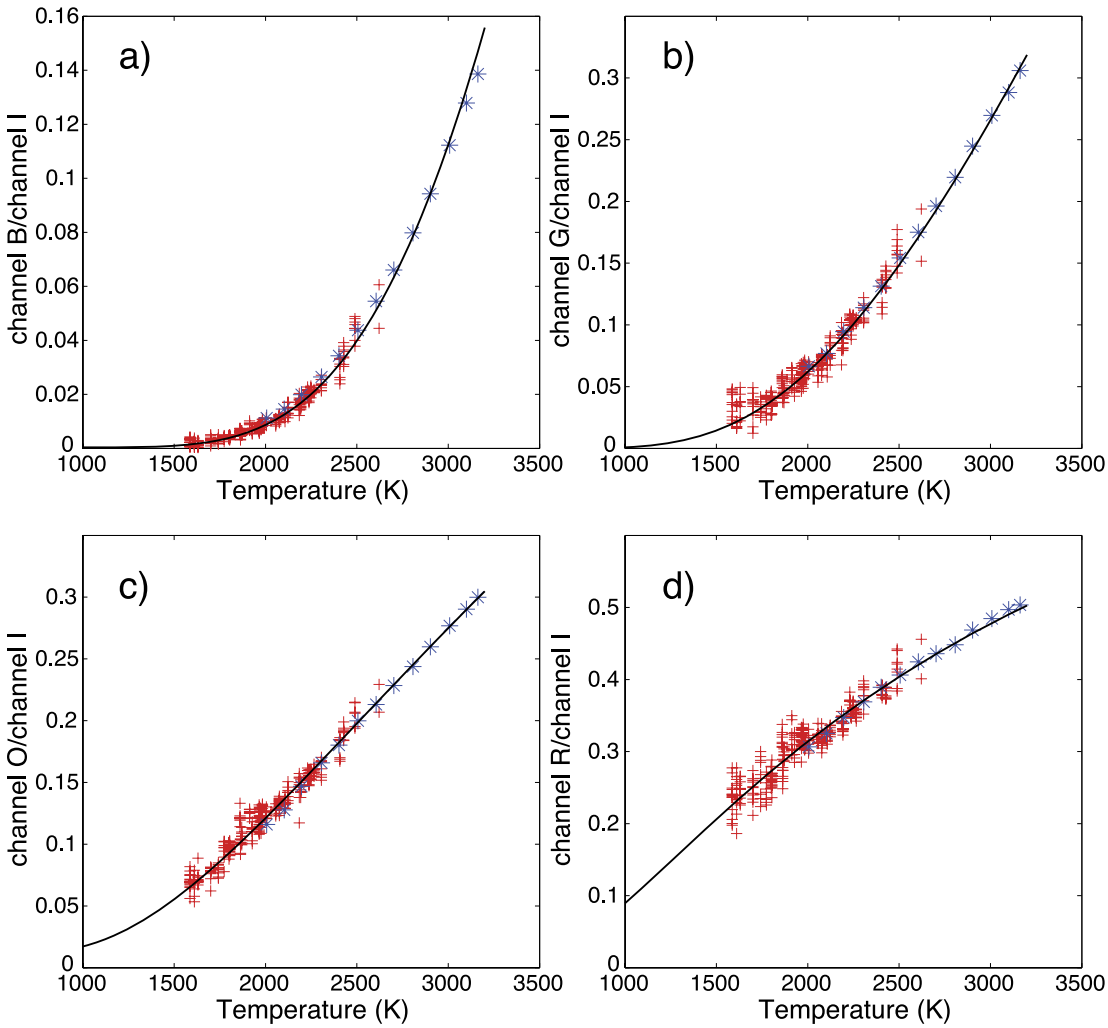

FIG. 3. Calibration of intensity ratios from theoretical calculations (black curve) and the tungsten standard lamp (blue asterisk, temperature read from the lamp controller), and comparison with measured laser-heated hotspot (red cross, temperature read from the CCD spectrometer). NDF is out of the optical path during this specific calibration and laser heating. (a) Intensity ratio between channel B and channel I. (b) Intensity ratio between channel G and channel I. (c) Intensity ratio between channel O and channel I. (d) Intensity ratio between channel R and channel I. The intensities of different channels are measured simultaneously during the experiment. Wavelength ranges for each channel provided in the text and Fig. 2.

different channels at different temperatures are calculated from the integration of Planck's black body radiation function and the transmission band of each channel. The influence of the optical system is corrected by fitting the calculated theoretical relative ratio curve to the measured relative ratios from the calibration. In the experiments, the temperature is calculated so that the residual function

$$R = \sum_{i=1}^{4} c_i \left(\left(\frac{I_i}{I_{ref}} \right)_{measure} - \left(\frac{I_i(T)}{I_{ref}(T)} \right)_{theory} \right)^2, \quad (1)$$

where

$$c_i = \left(\frac{\sum I_i(T)}{I_i(T)} \right)^2_{theory} \quad (2)$$

is minimized. In this formula, T is the temperature, I_i is the signal from channel i (unit: V), $c(i)$ is the weight constant of channel i so that the temperature determination does not weigh too much on one specific channel in the measured temperature range. Depending on the intensities of all channels, $c(i)$ varies in different experiments. I_{ref} is the reference channel's intensity, which has the largest signal-to-noise ratio. In our measurements, the reference channel is the infrared channel (channel I). Using a computer acquisition sequence, the temperature is calculated and recorded as the experiment proceeds. Calibration of the CCD-based spectrometer at beamline 3-ID-B is also achieved using similar procedures.

Three different heating runs on Fe and $Fe_{0.9}Ni_{0.1}$ samples, prepared in different DACs, are shown in Fig. 4 to illustrate the point that the temperatures determined by FasTeR are in good agreement with those determined from the conventional CCD-based spectrometer in the explored range of 1500–3000 K. For the temperature error of each reported temperature from the FasTeR system, we consider three contributions. One contribution is the dark current fluctuation of each PMT, which is on the order of 0.2 mV. The dark current fluctuation is calculated so that the residual function

$$R' = \sum_{i=1}^{4} c_i \left(\left(\frac{I_i + \Delta I}{I_{ref} - \Delta I} \right)_{measure} - \left(\frac{I_i(T + \Delta T)}{I_{ref}(T + \Delta T)} \right)_{theory} \right)^2 \quad (3)$$

is minimized. In this formula, $\Delta I = 0.2$ mV, ΔT is the dark current fluctuation, and the other parameters are the same as in formula (1). The dark current fluctuation is the error of a single FasTeR reading, and it varies with the signal intensity of each PMT. The higher the intensity is, the smaller the dark current contribution is. At ~1500 K, the dark current fluctuation can be as high as 300 K, whereas at temperatures higher than 2000 K, the dark current fluctuation is usually less than 10 K. In certain experiments, such as melting point determinations (see Sec. III), the scattering error of the temperature determined by FasTeR is considered as the second contribution to the temperature error. While different types of data are recorded simultaneously at one rate, such as the integrated SMS delayed counts, ion chamber intensities, laser power, and CCD temperature every few seconds, FasTeR temperatures are recorded every ~10 ms. For example, the FasTeR temperature corresponding to a particular SMS delayed count is the average of ~300 FasTeR readings, and the standard deviation is reported as the scattering error. The scattering error is

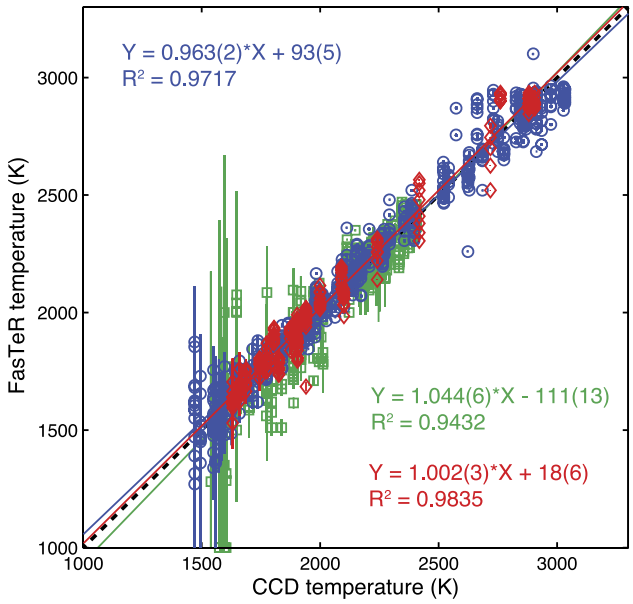

FIG. 4. Comparison between the temperatures read by the CCD spectrometer (horizontal axis) and FasTeR (vertical axis) for three different heating runs. The samples are $Fe_{0.9}Ni_{0.1}$ at P_{300K} = 29 ± 2 GPa (blue circles), $Fe_{0.9}Ni_{0.1}$ at P_{300K} = 66 ± 3 GPa (green squares), and Fe at P_{300K} = 28 ± 2 GPa (red diamonds). The CCD spectrometer temperature's error is estimated to be 100 K [1,19,34] (not shown here for clarity), and the FasTeR temperature's error plotted here is the dark current fluctuation. The scattering error is then determined from the distribution of measured temperatures at a given CCD-determined temperature. Dashed line: Y=X identity line. Solid lines: linear regressions of the three datasets. Values in parentheses indicate the uncertainty in the last significant digit.

experiment-dependent. Both the dark current fluctuation and the scattering error are considered in the final temperature error determination. The third contribution we consider is the effect of chromatic aberration (~10 K, discussed in Sec. II B). During melting experiments at high pressures, the scattering error dominates for each FasTeR temperature. Typically, the largest differences between FasTeR and CCD-based temperatures are found at lower temperatures and temperatures near the melting point of the material. Due to FasTeR's large dynamic range, one does not need to change its integration time during heating. FasTeR's working temperature range can be adjusted by changing the gain of the PMTs.

D. FasTeR sampling frequency

As its name implies, the FasTeR spectrometer features a temperature reading rate much faster than most conventional CCD-based systems. Currently, temperatures are well-determined at a readout rate of 100 Hz, up to 300 times faster than the conventional CCD at the same beamline. We compare the temperature readout rates between FasTeR and the conventional CCD spectrometer. Temperatures are recorded continuously by both systems during any given heating run, however more time is required to readout the intensities of a conventional CCD-based system. The time interval between two FasTeR readings is ~10 ms, whereas the time interval between two CCD readings is ~3 s. During one example melting experimental run, FasTeR records ~30 000 measurements

(downstream side), while only 46 measurements per side from the CCD are recorded (92 measurements in total).

We have also tested the sampling frequency of FasTeR with an optical chopper. In this test, a 3000 ± 100 K illuminator is placed behind a 200 μm pinhole, and the pinhole is located at the focal position of the FasTeR system. An optical chopper is placed in front of the pinhole, and interrupts the light from the pinhole periodically. The frequency of the optical chopper is adjustable in the range of 20–100 Hz. One can see that the sampling frequency of FasTeR can clearly distinguish the 100 Hz signal from the chopper (Fig. 5). In this set-up, the sampling frequency of FasTeR reaches ~400 Hz, as determined from the number of measured temperatures divided by the duration of the measurement (recorded in the FasTeR data file). The fluctuations and spikes in the signal arise from the phase shift between the PMTs and optical chopper (~1 ms) and of each PMT (~1 μs) that is recorded in series during an experiment. In continuous wave laser-heating scenarios, the temperature fluctuation rate can be on the order of 10^4 K/s,[13] which could come from large changes in thermal conductivity or changes in the reflectivity of the sample during melting.[12,13,17] In this study, we observe a transient temperature fluctuation: The temperature of the sample changes by about 600 K within 2 s (Fig. 6). This temperature fluctuation indicates a change in the coupling between the laser and the sample and is likely associated with melting.[17] FasTeR catches this rapid temperature fluctuation, whereas the conventional CCD spectrometer does not, because this temperature fluctuation coincides with the data transferring period between the two CCD readings. This case demonstrates that the FasTeR spectrometer is capable of capturing such fluctuations and thus obtaining a more accurate assessment of the sample's temperature during time-resolved experiments.

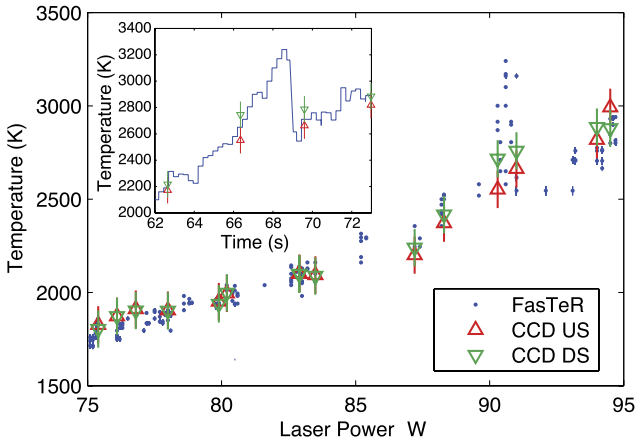

FIG. 6. Transient temperature fluctuation as a function of laser power captured by the FasTeR system but not the CCD spectrometer. Temperatures read by the FasTeR system (blue dots, looking at the downstream side) and the CCD spectrometer (upstream side: red normal triangles; downstream side: green reversed triangles). Inset: temperature as a function of time, zoomed in to the rapid fluctuation (blue curve: FasTeR temperatures). The plateaus of the FasTeR temperatures come from the select time resolution of the analog-digital converter for this specific experiment (5 Hz). The FasTeR system's sampling rate is 100 Hz. Sample: *fcc*-$Fe_{0.9}Ni_{0.1}$, P_{300K} = 39 ± 2 GPa.

E. Simulating FasTeR

In order to understand the new FasTeR instrument in terms of its performance, response, and design modifications, we have performed several simulations. To this end, we have

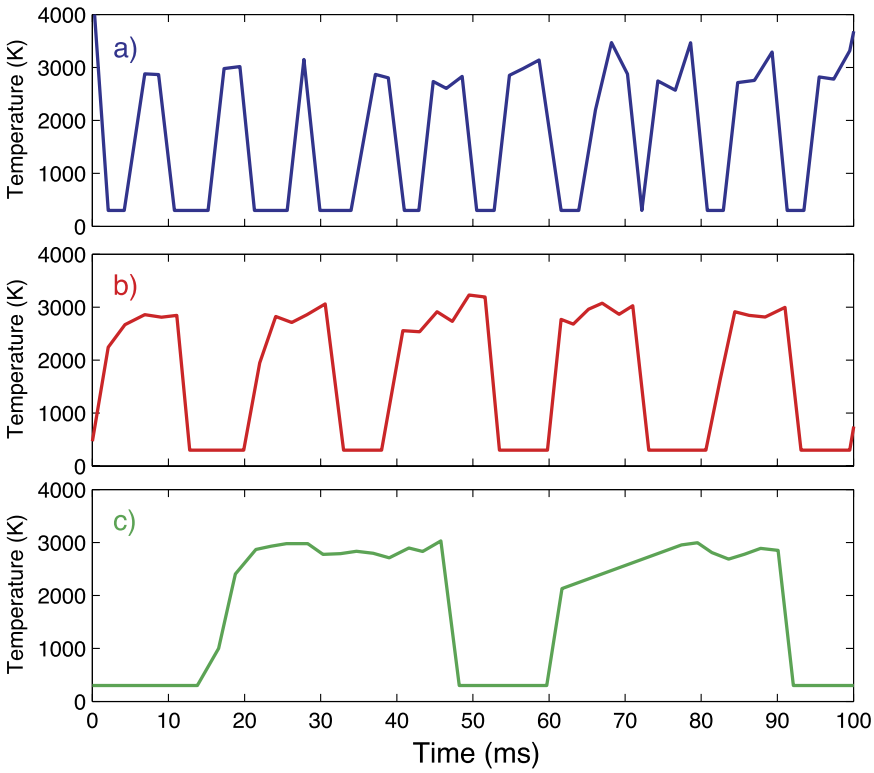

FIG. 5. FasTeR's time resolution tested with an optical chopper. The light source's temperature is 3000 ± 100 K. (a) Chopper frequency = 100 Hz. (b) Chopper frequency = 50 Hz. (c) Chopper frequency = 20 Hz. The fine structure of the temperature readouts is mostly due to the fact that the PMTs are not exactly synchronized (temporal offset ~1 ms) with the optical chopper (temporal offset ~1 ms).

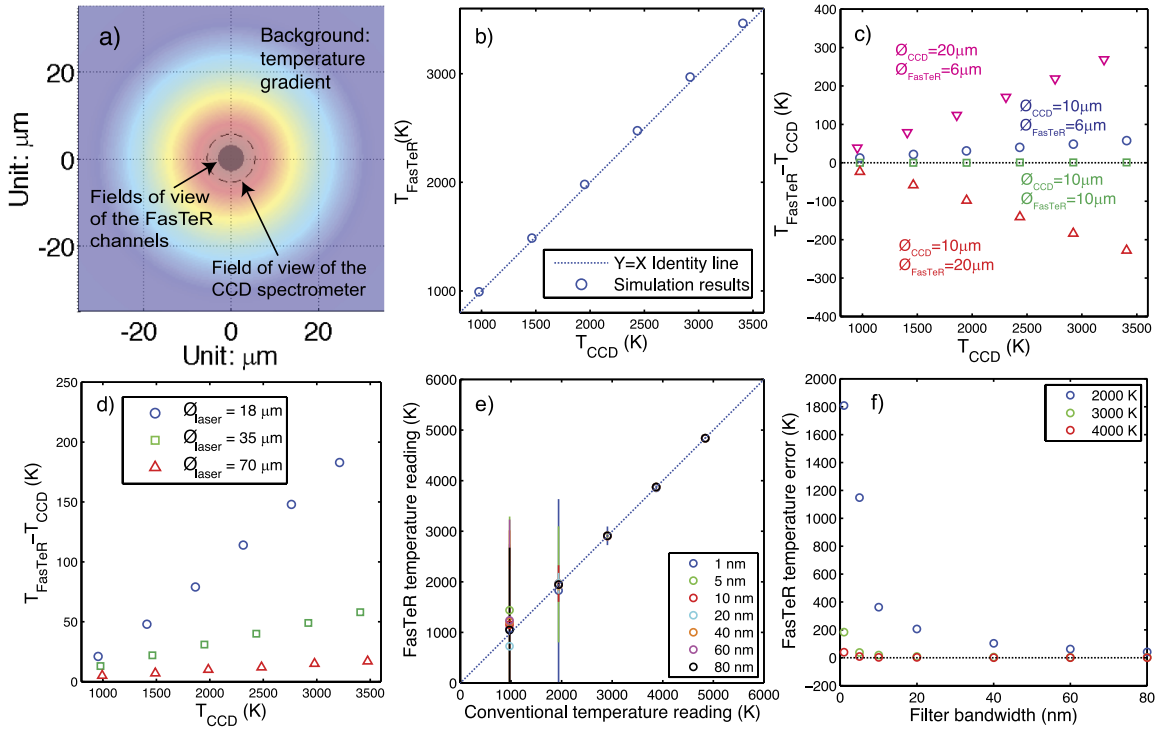

FIG. 7. (a) One example of the simulation conditions: $Ø_{laser}$ = 35 μm (background), $Ø_{CCD}$ = 10 μm (dashed circle at the center), $Ø_{FasTeR}$ = 6 μm (grey filled circle at the center). (b) Comparison of temperatures determined by FasTeR and the CCD spectrometer from simulations using SIMFaster. Simulation conditions are the same as in (a). Dashed line is the Y=X identity line. Temperature differences are the result of the mismatch in field of views for FasTeR and the CCD spectrometers. (c) Influence of selected variations of the $Ø_{FasTeR}$ and the $Ø_{CCD}$. The $Ø_{laser}$ is fixed at 35 μm. Blue circles: $Ø_{CCD}$ = 10 μm, $Ø_{FasTeR}$ = 6 μm. Green squares: $Ø_{CCD}$ = 10 μm, $Ø_{FasTeR}$ = 10 μm. Red triangles up: $Ø_{CCD}$ = 10 μm, $Ø_{FasTeR}$ = 20 μm. Magenta triangles down: $Ø_{CCD}$ = 20 μm, $Ø_{FasTeR}$ = 6 μm. (d) Influence of varying the $Ø_{laser}$. The $Ø_{CCD}$ is fixed at 10 μm, and the $Ø_{FasTeR}$ is fixed at 6 μm. Blue circles: $Ø_{laser}$ = 35 μm. Green squares: $Ø_{laser}$ = 18 μm. Red triangles up: $Ø_{laser}$ = 70 μm. (e) and (f) Comparison of the temperature reading (e) and error (f) using different channel bandwidths. The $Ø_{CCD}$ and the $Ø_{FasTeR}$ are fixed at 10 μm, $Ø_{laser}$ = 35 μm, and all detectors share the same noise level.

developed simulation software called SIMFaster, which is written in MatLab. SIMFaster uses the channel transmission of the FasTeR system, $Ø_{laser}$, $Ø_{FasTeR}$, and $Ø_{CCD}$ as its inputs (Fig. 7(a)). For simulating the temperature determined from FasTeR, SIMFaster convolves the black body radiation curve with the channel transmissions, integrates over $Ø_{FasTeR}$ to obtain the intensity of each detector, and fits the intensity ratios between different channels to calculate the temperature.

We present several simulations with variations of the various Ø. We first start with a simulation using the typical values for the various Ø in our experimental set-up and optimized conditions ($Ø_{laser}$ = 35 μm, $Ø_{CCD}$ = 10 μm, $Ø_{FasTeR}$ = 6 μm, where FasTeR and the CCD spectrometer are aligned to the center of the hotspot) (Figs. 7(a) and 7(b)). One can see that the temperature offset between the FasTeR system and the CCD spectrometer is temperature dependent, where the temperature difference is about 60 K at 3000 K. These offsets are due to the difference between the $Ø_{FasTeR}$ and the $Ø_{CCD}$ (Fig. 7(c)). When there is no difference between $Ø_{FasTeR}$ and the $Ø_{CCD}$, there is no temperature offset. Similarly, the $Ø_{laser}$ also affects the temperature offset when the $Ø_{FasTeR}$ and the $Ø_{CCD}$ are not equal (Fig. 7(d)). The smaller the $Ø_{laser}$ is, the larger the temperature offset will be. Such simulations are necessary to evaluate if and when any of the components drift during an experiment.

Another important application of the simulation software is the assessment of system design changes. To this end, we assess the influence of the transmission bandwidth of the optical filter system (Figs. 7(e) and 7(f)). Using SIMFaster, we assume that both the $Ø_{FasTeR}$ and the $Ø_{CCD}$ are 10 μm, $Ø_{laser}$ = 35 μm, and all the detectors share the same noise level. We adjust the detector noise level so that the temperature error is 100 K at max(T_{laser}) = 2000 K when the transmission bandwidth = 40 nm, which is close to our experimental condition. Numerical simulation shows that narrowing the transmission bandwidth has little effect on the temperature reading (Fig. 7(e)), but will significantly increase the error of temperature determination (Fig. 7(f)), because the total intensity collected by the detector is proportional to the transmission bandwidth. Thus, it would only make sense to use narrower bandwidth filters (less than about 40 nm) for experiments that involve a much brighter thermal flux than those presented here.

III. MELTING OF $^{57}Fe_{0.9}Ni_{0.1}$ AT HIGH PRESSURE

As a demonstration of the FasTeR system, we have determined the melting point of $^{57}Fe_{0.9}Ni_{0.1}$ at $P_{300K} = 29 \pm 2$ GPa. The high pressure environment is provided by a symmetric-type piston cylinder diamond-anvil cell. Two Type-I diamonds with 300 μm culets are mounted and aligned to form the anvils. A Re gasket is pre-indented to ~45 μm thick, and a 110 μm diameter hole is drilled in the center of the pre-indention using a laser drilling system located at GSE-CARS, APS. A

95% isotopically enriched $^{57}Fe_{0.9}Ni_{0.1}$ foil with a thickness of 15 μm is cut into 60 × 80 μm^2 rectangular sections and cleaned. Dehydrated KCl is pressed into transparent flakes and loaded together with the $^{57}Fe_{0.9}Ni_{0.1}$ foil in a sandwich configuration into the Re gasket. The KCl serves as both a pressure-transmitting medium and a thermal insulator. The sample is dehydrated in a vacuum furnace at 100 °C. A few ruby spheres (~10 μm in diameter) are placed away from the sample and used as pressure markers.[37] The *in-situ* XRD patterns collected at 3-ID-B indicate that the pressurized $^{57}Fe_{0.9}Ni_{0.1}$ sample is hexagonally close packed (*hcp*) at 300 K. We constrain the sample's pressure at ambient temperature using both ruby fluorescence and *in-situ* X-ray diffraction. The pressure of this sample at 300 K is thus determined to be 29 ± 2 GPa. For all the example heating runs (e.g., Figs. 4 and 6), the samples were prepared and analyzed in this fashion.

The SMS experiments to determine melting are similar to those described in Jackson *et al.*[21] First, the X-ray and laser focal areas are aligned. Then, the sample pressure at 300 K is constrained by collecting *in-situ* X-ray diffraction images and using *hcp* Fe's equation of state.[38] The thermal pressure of the sample is constrained from the diffraction patterns with and without laser heating, where we use *fcc* Fe's equation of state at high temperatures.[39] After an XRD image is collected at 300 K, a 300 K SMS spectrum is collected at the location where the melting measurement is going to be carried out. We then preheat the sample and balance the upstream and downstream temperatures at around 1500 K, so that the sample is heated uniformly. Then, we collect a SMS spectrum at this temperature. The hot SMS spectrum provides the effective thickness of the sample at a reference temperature and is used in the fitting routine of the data to determine the melting point. Immediately after collecting the high temperature SMS spectrum, we begin the computer-controlled sequence of a melting run. In this sequence, the laser power is ramped up every 3 s and many parameters are recorded, such as the integrated SMS delayed counts, laser power, the intensities of the ion chambers, and the temperatures from FasTeR and the CCD spectrometer. The intensity recorded by ion chamber #3 (IC3) is proportional to the total incident X-ray intensity. The integrated SMS delayed signal over 3 s is then normalized with respect to the reading of IC3. More details of the data analysis can be found in Jackson *et al.*[21] The temperature and the normalized delayed counts are plotted as a function of laser power in Fig. 8. Immediately after a melting run is completed and the laser power is shut off, the sample is scanned in both x and y directions to verify proper alignment of the X-ray and IR laser focal areas. Finally, an ambient temperature SMS spectrum and an XRD pattern are collected at the same location to constrain the effective thickness and sample pressure after the melting run.

The temperature of the sample is recorded simultaneously by the FasTeR system while ramping up the laser power. Since the FasTeR system has a sampling frequency much higher than that for SMS, the FasTeR temperature corresponding to each SMS data point is reported as the average of the FasTeR temperature during the integration time (3 s/pt). The CCD temperature corresponding to each SMS data point is reported as the average of the upstream and the downstream CCD temperatures. In each step, there is one upstream CCD temperature and one downstream CCD temperature recorded. The CCD temperatures are fitted using the SpecT code.[1]

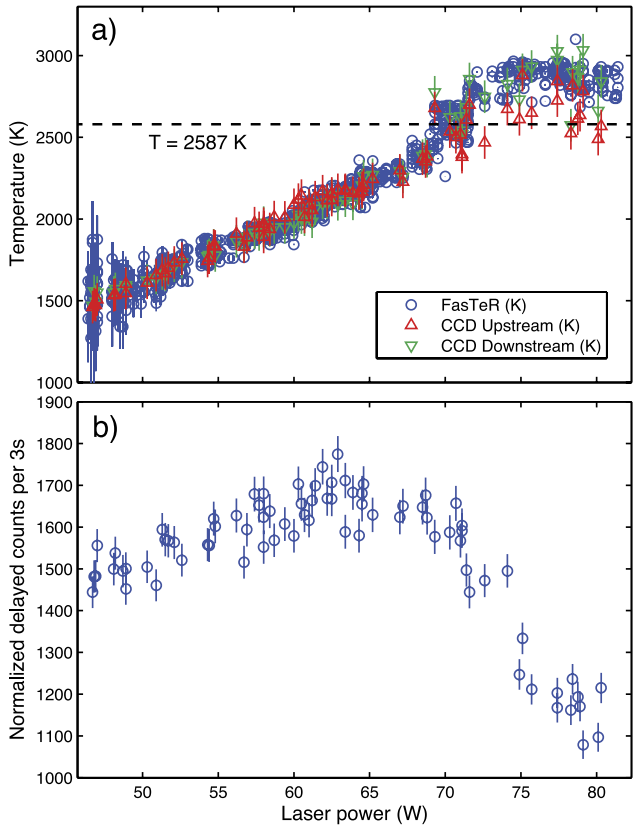

FIG. 8. Temperature and normalized delayed counts as functions of the laser power. (a) Temperature as a function of the laser power. Blue circles: temperatures read by the FasTeR system. Red and green triangles: best-fit temperatures, determined using the SpecT code,[1] from the upstream and downstream directions. FasTeR error bar: dark current fluctuation (see text). CCD spectrometer error bar: 100 K. (b) Normalized SMS delayed counts per 3 s as a function of the laser power. The delayed counts are normalized with respect to the incident X-ray intensity. Error bars are given by the square-root of measured delayed counts. The laser power is read from the laser controller module. The laser output power fluctuation is within 0.5%. The sample's pressure at 300 K is P_{300K} = 29 ± 2 GPa. Note that the melting point of KCl at 30 GPa is 3410 ± 50 K.[35]

The melting point is determined by fitting the normalized SMS delayed signal as a function of the sample temperature using the SIMX module of the MINUTI software package[36] (Fig. 9). The melting temperatures with the best fit are 2587 K for the FasTeR data and 2534 for the CCD data, with fitting errors of 22 K and 32 K, respectively. We report the error of the melting point determined from FasTeR as the quadrature sum of the SIMX fitting error (22 K), the average axial surface temperature difference determined from the CCD (35 K), the chromatic aberration (10 K), and the appropriate level of uncertainty assessed from the spectroradiometric method and detailed balance principle (100 K).[40] The error for the melting temperature determined from the CCD temperatures is computed similarly. Thus, the melting temperatures are 2587 ± 109 K for the FasTeR data, and 2534 ± 112 K for the CCD data.

If one uses the laser power vs. temperature approach to determine melting, i.e., locating the temperature plateau or change in trend as a function of laser power,[41,42] a value of

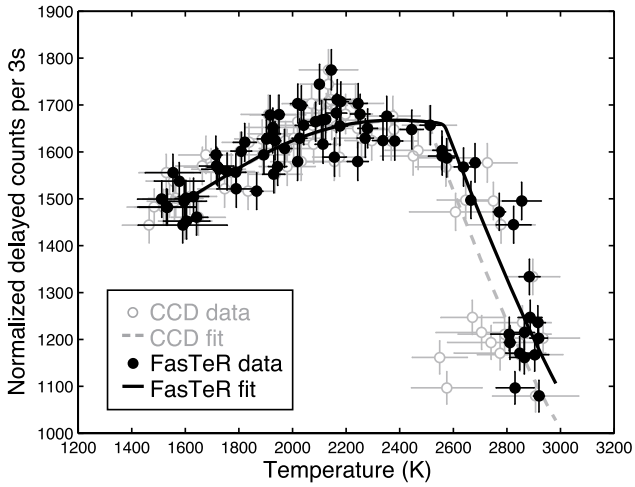

FIG. 9. Determining the melting temperature of $Fe_{0.9}Ni_{0.1}$ at P_{300K} = 29 ± 2 GPa. Black solid dots: temperatures determined from the FasTeR system. Grey empty circles: temperatures determined from the CCD spectrometer. Black curve: best-fit theoretical curve using the FasTeR data. Grey dashed curve: best-fit theoretical curve using the CCD data. For the FasTeR data, ~300 measurements are represented in each temperature value plotted. The error bars of the temperatures are the scattering uncertainties of the ~300 FasTeR measurements. Each CCD data point represents the average of the upstream and the downstream CCD temperatures in one measurement, and its error bar is assumed to be the quadrature sum of the front/back temperature gradient and the uncertainty of the temperature reading. The best-fit melting points are 2587 ± 109 K for the FasTeR data, and 2534 ± 112 K for the CCD data. The best-fit theoretical curves, the melting points, and their errors come from SIMX.[36] See text for details on the fitting procedure.

2864 ± 219 K is obtained from FasTeR temperatures. This melting point criteria is based on the premise that the molten phase likely has a higher thermal conductivity or reflectivity than the solid phase.[17] Because the laser's spot size is typically larger than the X-ray's sampling volume and provided there are finite temperature/pressure gradients, the plateau criteria will likely overestimate the melting temperature, as it requires a relatively large volume of the sample to change its thermal conductivity or reflectivity. The method we present here, that is monitoring the atomic dynamics using synchrotron Mössbauer spectroscopy, requires that only the material in the sampled X-ray volume melt, which is a small fraction of the laser's spot size.

We compare our melting point of $^{57}Fe_{0.9}Ni_{0.1}$ at P_{300K} = 29 ± 2 GPa with previous studies on pure Fe and an Fe-Ni-Si alloy at similar pressures. Our value of 2587±109 K is close to the reported melting point of pure Fe from Shen *et al.*[43] (2550 ± 50 K at P_{300K} = 28 GPa) and Jackson *et al.*[21] (2500 ± 115 K at P_{300K} = 28 ± 3 GPa), but higher than the melting point reported by Boehler *et al.* for pure Fe (~2400 K at ~30 GPa).[41] Our melting point of $^{57}Fe_{0.9}Ni_{0.1}$ is higher than the melting point of $Fe_{0.78}Ni_{0.04}Si_{0.18}$ (Morard *et al.*,[44] 2440 ± 150 K at P_{300K} = 28 ± 1 GPa), although within mutual reported uncertainties.

IV. CONCLUSIONS

A multi-wavelength fast temperature readout spectrometer named FasTeR has been developed at beamline 3-ID-B of the Advanced Photon Source. Working together with nuclear resonant scattering and X-ray diffraction techniques and double-sided laser-heating in the diamond-anvil cell, the FasTeR spectrometer consists of an array of photomultiplier tubes and optical dichroic filters. The benefits of this system are that it features a fast readout rate, high sensitivity, large dynamic range, well-constrained focus, and a relatively simple and inexpensive design. A software tool, SIMFaster, has been developed to simulate FasTeR and assess design configurations.

Example heating runs on different samples have been demonstrated. In this study, experiments were conducted up to about 3000 K, and we see no barrier for the FasTeR spectrometer to determine temperatures higher than 3000 K. Well calibrated, the temperatures determined outside the vicinity of melting from FasTeR are generally in good agreement with results from the conventional CCD spectrometer.

Dedicated to monitoring the atomic dynamics under extreme conditions, FasTeR overcomes some of the drawbacks of a conventional CCD-based system. Specifically, FasTeR is capable of capturing transient temperature fluctuations, at least on the order of 300 K/s, due to its relatively large dynamic range (~10^6). FasTeR's maximum temperature readout rate sampled in this study is 400 Hz, orders of magnitude higher than the CCD-based temperature reading system at the same beamline. We have combined FasTeR with synchrotron Mössbauer spectroscopy to determine the melting temperature of $^{57}Fe_{0.9}Ni_{0.1}$ at high pressure.

The characteristics of FasTeR would also benefit temperature determinations for studies that utilize ultra-fast techniques, such as time-domain thermoreflectance,[22–24] thermal diffusivity,[25] measurements using the dynamic diamond-anvil cell,[26] pulsed laser-heating,[27,28] and measurements utilizing high-speed periodic shutters.[29] The principle design of the FasTeR system is also suitable for shock/ramp compression experiments.[8,9,30]

ACKNOWLEDGMENTS

We thank G. Shen, V. B. Prakapenka, M. Rivers, Y. Meng, W. Bi, A. Alatas, and B. Chen for useful discussions and help with commissioning of this system. We are grateful to C. A. Murphy for synthesizing the $^{57}Fe_{0.9}Ni_{0.1}$ sample. We thank the California Institute of Technology and NSF (EAR-1316362) for support of this research, GSE-CARS and HP-CAT for the use of the laser drilling and the ruby fluorescence systems, and an anonymous reviewer for his/her thoughtful and constructive comments. Use of the Advanced Photon Source is supported by the U.S. D.O.E., O.S., O.B.E.S. (DE-AC02-06CH11357). Sector 3 operations are supported in part by COMPRES under NSF Cooperative Agreement EAR 06-49658.

[1]G. Shen, M. L. Rivers, Y. Wang, and S. R. Sutton, "Laser heated diamond cell system at the advanced photon source for in situ x-ray measurements at high pressure and temperature," Rev. Sci. Instrum. **72**(2), 1273–1282 (2001).
[2]G. Shen, V. B. Prakapenka, P. J. Eng, M. L. Rivers, and S. R. Sutton, "Facilities for high-pressure research with the diamond anvil cell at GSECARS," J. Synchrotron Radiat. **12**(5), 642–649 (2005).
[3]Y. Meng, G. Shen, and H. K. Mao, "Double-sided laser heating system at HPCAT for in situ x-ray diffraction at high pressures and high temperatures," J. Phys.: Condens. Matter **18**(25), S1097 (2006).
[4]V. B. Prakapenka, A. Kubo, A. Kuznetsov, A. Laskin, O. Shkurikhin, P. Dera, M. L. Rivers, and S. R. Sutton, "Advanced flat top laser heating system for

high pressure research at GSECARS: Application to the melting behavior of germanium," High Pressure Res. **28**(3), 225–235 (2008).
[5]W. A. Bassett, A. H. Shen, M. Bucknum, and I.-M. Chou, "A new diamond anvil cell for hydrothermal studies to 2.5 GPa and from -190 to 1200 °C," Rev. Sci. Instrum. **64**(8), 2340–2345 (1993).
[6]Z. Du, L. Miyagi, G. Amulele, and K. K. M. Lee, "Efficient graphite ring heater suitable for diamond-anvil cells to 1300 K," Rev. Sci. Instrum. **84**(2), 024502 (2013).
[7]C.-S. Zha, K. Mibe, W. A. Bassett, O. Tschauner, H.-K. Mao, and R. J. Hemley, "P-V-T equation of state of platinum to 80 GPa and 1900 K from internal resistive heating/x-ray diffraction measurements," J. Appl. Phys. **103**(5), 054908 (2008).
[8]P. Loubeyre, P. M. Celliers, D. G. Hicks, E. Henry, A. Dewaele, J. Pasley, J. Eggert, M. Koenig, F. Occelli, K. M. Lee, R. Jeanloz, D. Neely, A. Benuzzi-Mounaix, D. Bradley, M. Bastea, S. Moon, and G. W. Collins, "Coupling static and dynamic compressions: First measurements in dense hydrogen," High Pressure Res. **24**(1), 25–31 (2004).
[9]R. Jeanloz, P. M. Celliers, G. W. Collins, J. H. Eggert, K. K. M. Lee, R. S. McWilliams, S. Brygoo, and P. Loubeyre, "Achieving high-density states through shock-wave loading of precompressed samples," Proc. Natl. Acad. Sci. U. S. A. **104**(22), 9172–9177 (2007), available URL: http://www.pnas.org/content/104/22/9172.abstract.
[10]R. Boehler, "High-pressure experiments and the phase diagram of lower mantle and core materials," Rev. Geophys. **38**(2), 221–245, doi:10.1029/1998RG000053 (2000).
[11]A. J. Campbell, "Measurement of temperature distributions across laser heated samples by multispectral imaging radiometry," Rev. Sci. Instrum. **79**(1), 015108 (2008).
[12]R. Jeanloz and D. L. Heinz, "Experiments at high temperature and pressure: Laser heating through the diamond cell," J. Phys. Colloques **45**(C8), 83–92 (1984).
[13]R. Jeanloz and A. Kavner, "Melting criteria and imaging spectroradiometry in laser-heated diamond-cell experiments," Philos. Trans. R. Soc., A **354**(1711), 1279–1305 (1996).
[14]A. Dewaele, M. Mezouar, N. Guignot, and P. Loubeyre, "Melting of lead under high pressure studied using second-scale time-resolved x-ray diffraction," Phys. Rev. B **76**, 144106 (2007).
[15]A. Dewaele, M. Mezouar, N. Guignot, and P. Loubeyre, "High melting points of tantalum in a laser-heated diamond anvil cell," Phys. Rev. Let. **104**, 255701 (2010).
[16]S. Anzellini, A. Dewaele, M. Mezouar, P. Loubeyre, and G. Morard, "Melting of iron at Earth's inner core boundary based on fast X-ray diffraction," Science **340**(6131), 464–466 (2013).
[17]Z. M. Geballe and R. Jeanloz, "Origin of temperature plateaus in laser-heated diamond anvil cell experiments," J. Appl. Phys. **111**(12), 123518 (2012).
[18]D. L. Heinz, J. S. Sweeney, and P. Miller, "A laser heating system that stabilizes and controls the temperature: Diamond anvil cell applications," Rev. Sci. Instrum. **62**(6), 1568–1575 (1991).
[19]J. Zhao, W. Sturhahn, J. F. Lin, G. Shen, E. E. Alp, and H. K. Mao, "Nuclear resonant scattering at high pressure and high temperature," High Pressure Res. **24**(4), 447–457 (2004).
[20]Z. Du, G. Amulele, B. L. Robin, and K. K. M. Lee, "Mapping temperatures and temperature gradients during flash heating in a diamond-anvil cell," Rev. Sci. Instrum. **84**(7), 075111 (2013).
[21]J. M. Jackson, W. Sturhahn, M. Lerche, J. Zhao, T. S. Toellner, E. E. Alp, S. V. Sinogeikin, J. D. Bass, C. A. Murphy, and J. K. Wicks, "Melting of compressed iron by monitoring atomic dynamics," Earth Planet. Sci. Lett. **362**(0), 143–150 (2013).
[22]W.-P Hsieh, B. Chen, J. Li, P. Keblinski, and D. G. Cahill, "Pressure tuning of the thermal conductivity of the layered muscovite crystal," Phys. Rev. B **80**, 180302 (2009).
[23]B. Chen, W.-P. Hsieh, D. G. Cahill, D. R. Trinkle, and J. Li, "Thermal conductivity of compressed H_2O to 22 GPa: A test of the Leibfried-Schlömann equation," Phys. Rev. B **83**, 132301 (2011).
[24]D. A. Dalton, W.-P. Hsieh, G. T. Hohensee, D. G. Cahill, and A. F. Goncharov, "Effect of mass disorder on the lattice thermal conductivity of MgO periclase under pressure," Sci. Rep. **3**, 2400 (2013).
[25]P. Beck, A. F. Goncharov, V. V. Struzhkin, B. Militzer, H.-K. Mao, and R. J. Hemley, "Measurement of thermal diffusivity at high pressure using a transient heating technique," Appl. Phys. Lett. **91**(18), 181914 (2007).
[26]N. Velisavljevic, S. Sinogeikin, R. Saavedra, R. S. Chellappa, A. Rothkirch, D. M. Dattelbaum, Z. Konopkova, H.-P. Liermann, M. Bishop, G. M. Tsoi, and Y. K. Vohra, "Time-resolved x-ray diffraction and electrical resistance measurements of structural phase transitions in zirconium," J. Phys.: Conf. Ser. **500**(3), 032020 (2014).
[27]A. F. Goncharov, V. B. Prakapenka, V. V. Struzhkin, I. Kantor, M. L. Rivers, and D. A. Dalton, "X-ray diffraction in the pulsed laser heated diamond anvil cell," Rev. Sci. Instrum. **81**(11), 113902 (2010).
[28]C.-S. Yoo, H. Wei, R. Dias, G. Shen, J. Smith, J.-Y. Chen, and W. Evans, "Time-resolved synchrotron X-ray diffraction on pulse laser heated iron in diamond anvil cell," J. Phys.: Conf. Ser. **377**(1), 012108 (2012).
[29]T. S. Toellner, E. E. Alp, T. Graber, R. W. Henning, S. D. Shastri, G. Shenoy, and W. Sturhahn, "Synchrotron Mössbauer spectroscopy using high-speed shutters," J. Synchrotron Radiat. **18**(2), 183–188 (2011).
[30]G. A. Lyzenga and T. J. Ahrens, "Multiwavelength optical pyrometer for shock compression experiments," Rev. Sci. Instrum. **50**(11), 1421–1424 (1979).
[31]L. Gao, B. Chen, M. Lerche, E. E. Alp, W. Sturhahn, J. Zhao, H. Yavas, and J. Li, "Sound velocities of compressed Fe3C from simultaneous synchrotron x-ray diffraction and nuclear resonant scattering measurements," J. Synchrotron Radiat. **16**(6), 714–722 (2009).
[32]W. Sturhahn, "Nuclear resonant spectroscopy," J. Phys.: Condens. Matter **16**(5), S497–S530 (2004).
[33]T. S. Toellner, "Monochromatization of synchrotron radiation for nuclear resonant scattering experiments," Hyperfine Interact. **125**(1-4), 3–28 (2000).
[34]J.-F. Lin, W. Sturhahn, J. Zhao, G. Shen, H.-K. Mao, and R. J. Hemley, "Absolute temperature measurement in a laser-heated diamond anvil cell," Geophys. Res. Lett. **31**(14), L14611, doi:10.1029/2004GL020599 (2004).
[35]R. Boehler, M. Ross, and D. B. Boercker, "High-pressure melting curves of alkali halides," Phys. Rev. B **53**, 556–563 (1996).
[36]MINUTI free software at www.nrixs.com.
[37]H.-K. Mao, J. Xu, and P. M. Bell, "Calibration of the ruby pressure gauge to 800-kbar under quasi-hydrostatic conditions," J. Geophys. Res., [Solid Earth Planets] **91**(B5), 4673–4676, doi:10.1029/JB091iB05p04673 (1986).
[38]A. Dewaele, P. Loubeyre, F. Occelli, M. Mezouar, P. I. Dorogokupets, and M. Torrent, "Quasihydrostatic equation of state of iron above 2 mbar," Phys. Rev. Lett. **97**, 215504 (2006).
[39]T. Komabayashi and Y. Fei, "Internally consistent thermodynamic database for iron to the earth's core conditions," J. Geophys. Res., [Solid Earth] **115**(B3), B03202, doi:10.1029/2009JB006442 (2010).
[40]W. Sturhahn and J. M. Jackson, "Geophysical applications of nuclear resonant scattering," in *Advances in High-Pressure Mineralogy: GSA Special Paper 421* (Geological Society of America, Boulder, Colorado, 2007), pp. 157–174.
[41]R. Boehler, N. von Bargen, and A. Chopelas, "Melting, thermal expansion, and phase transitions of iron at high pressures," J. Geophys. Res., [Solid Earth] **95**(B13), 21731–21736, doi:10.1029/JB095iB13p21731 (1990).
[42]R Boehler, "Temperatures in the earth's core from melting-point measurements of iron at high static pressures," Nature **363**(6429), 534–536 (1993).
[43]G. Shen, V. B. Prakapenka, M. L. Rivers, and S. R. Sutton, "Structure of liquid iron at pressures up to 58 GPa," Phys. Rev. Lett. **92**, 185701 (2004).
[44]G. Morard, D. Andrault, N. Guignot, J. Siebert, G. Garbarino, and D. Antonangeli, "Melting of Fe-Ni-Si and Fe-Ni-S alloys at megabar pressures: Implications for the core-mantle boundary temperature," Phys. Chem. Miner. **38**(10), 767–776 (2011).